

Near-infrared photometry of Y dwarfs: low ammonia abundance and the onset of water clouds

S. K. Leggett¹

sleggett@gemini.edu

Caroline V. Morley²

M. S. Marley³

and

D. Saumon⁴

ABSTRACT

We present new near-infrared photometry for seven late-type T dwarfs and nine Y-type dwarfs, and lower limit magnitudes for a tenth Y dwarf, obtained at Gemini Observatory. We also present a reanalysis of *H*-band imaging data from the Keck Observatory Archive, for an eleventh Y dwarf. These data are combined with earlier MKO-system photometry, *Spitzer* and *WISE* mid-infrared photometry, and available trigonometric parallaxes, to create a sample of late-type brown dwarfs which includes ten T9 — T9.5 dwarfs or dwarf systems, and sixteen Y dwarfs. We compare the data to our models which include updated H₂ and NH₃ opacity, as well as low-temperature condensate clouds. The models qualitatively reproduce the trends seen in the observed colors, however there are discrepancies of around a factor of two in flux for the Y0 – Y1 dwarfs, with $T_{\text{eff}} \approx 350 - 400$ K. At $T_{\text{eff}} \sim 400$ K, the problems could be addressed by significantly reducing the NH₃ absorption, for example by halving the abundance of NH₃ possibly by vertical mixing. At $T_{\text{eff}} \sim 350$ K, the discrepancy may be resolved by incorporating thick water clouds. The onset of these clouds might occur over a narrow range in T_{eff} , as indicated by the observed small change in 5 μm flux

¹Gemini Observatory, Northern Operations Center, 670 N. A'ohoku Place, Hilo, HI 96720, USA

²Department of Astronomy and Astrophysics, University of California, Santa Cruz, CA 95064, USA

³NASA Ames Research Center, Mail Stop 245-3, Moffett Field, CA 94035, USA

⁴Los Alamos National Laboratory, PO Box 1663, MS F663, Los Alamos, NM 87545, USA

over a large change in $J - W2$ color. Of the known Y dwarfs, the reddest in $J - W2$ are WISEP J182831.08+265037.8 and WISE J085510.83–071442.5. We interpret the former as a pair of identical 300 – 350 K dwarfs, and the latter as a 250 K dwarf. If these objects are ~ 3 Gyrs old, their masses are ~ 10 and ~ 5 Jupiter-masses respectively.

Subject headings: stars: brown dwarfs, Stars: atmospheres

1. Introduction

In 1995 the first definitive detection of an exoplanet orbiting a main-sequence star was announced (Mayor & Queloz 1995). In the same year, and in fact in the same edition of *Nature*, the first definitive detection of a brown dwarf (an object with insufficient mass for stable hydrogen-burning) was also announced (Nakajima et al. 1995). The detection of exoplanets continued at a rapid rate. However it was not until 1999 that more brown dwarfs were found, in the early data releases of the Sloan and 2MASS sky surveys (Burgasser et al. 1999, Strauss et al. 1999). The first exoplanet and brown dwarf discoveries were of relatively warm and massive sources. The exoplanets were of the “hot Jupiter” class, Jupiter-mass objects close to their star. The brown dwarfs were what are now known as mid-T class objects, with effective temperatures (T_{eff}) ≈ 1000 K, and mass ≈ 50 Jupiter-masses. Exoplanets that are much less massive and further from their host stars are now known, for example the planetary system around Kepler 11, with six planets at 0.1 – 0.5 AU, and masses as low as 2 Earth-masses (Lissauer et al. 2011). Similarly, cooler and lower mass brown dwarfs are now known (Cushing et al. 2011). The two populations have a significant degree of overlap, and brown dwarfs can show many observational similarities to directly-imaged exoplanets (Liu et al. 2013). There is active debate on how the formation mechanisms differ and relate to each other (e.g. Beichman et al. 2014 and references therein).

This paper continues our series of papers where we present new observations of brown dwarfs, and compare these data to state-of-the-art models calculated by members of the group. The known brown dwarf population has been extended to intrinsically fainter sources by sky surveys, most recently the Wide-field Infrared Survey Explorer (*WISE*; Wright et al. 2010). The models have become increasingly advanced using new pressure- (or collision-)induced H_2 absorption and NH_3 opacity (Saumon et al. 2012), and incorporating low-temperature condensate cloud decks (Morley et al., 2012, 2014). Our earlier papers include the verification of the reddening caused by silicate, sulphide and chloride clouds in L-, T- and Y-type dwarf atmospheres (Stephens et al. 2009, Leggett et al. 2013). Here we present new near-infrared photometry, and compare our dataset to models which include water clouds

(Morley et al. 2014).

2. Observations

In this paper we present new near-infrared photometry for seven late-type T dwarfs and nine Y-type dwarfs, obtained using the Gemini Observatory’s Near-Infrared Imager (NIRI, Hodapp et al. 2003) and FLAMINGOS-2 (Eikenberry et al. 2004). For a tenth Y dwarf, we present a reanalysis of H -band imaging data taken with the Keck Observatory’s NIRC2 near-infrared imager. We start this section with the presentation of new upper-limit fluxes (lower-limit magnitudes) for an eleventh Y dwarf.

2.1. zYJ limits for WD 0806–66B using GMOS-South and GSAOI

We observed WD 0806–66B, a very late-type brown dwarf companion to a white dwarf, at Gemini South using the Gemini Multi-Object Spectrograph (GMOS, Hook et al. 2004) and the Gemini South Adaptive Optics Imager (GSAOI, McGregor et al. 2004 and Carrasco et al. 2012). The primary, WD 0806–66, is also referenced in the literature as L 97-3, LTT 3059, NLTT 19008 and GJ 3483. While to our knowledge the label “WD” has never been used for an object that is not a white dwarf, this brown dwarf companion has been mainly referred to in the literature as WD 0806–66B, and we adopt that label here.

The brown dwarf was discovered in a search for common proper motion companions using *Spitzer* 4.5 μm images (Luhman, Burgasser & Bochanski 2011). Follow-up *Spitzer* 3.6 μm imaging and deep J -band imaging confirmed the source to be one of the coldest brown dwarfs known, with $T_{\text{eff}} \approx 350$ K (Luhman et al. 2012). Given the constraints on age imposed by the white dwarf, the mass of WD 0806–66B is $< 13 M_{\text{Jup}}$ (Rodríguez et al. 2011).

Deeper 1 μm imaging using the F110W filter and the Wide Field Camera 3 (WFC3) on the *Hubble Space Telescope* (*HST*) has now provided the first detection of the source in the near-infrared (Luhman et al. 2014b). Luhman et al. find $m_{110W} = 25.70 \pm 0.05$, and use observed spectra for T9 to Y0.5 dwarfs, as well as model-generated spectra, to estimate $m_{110W} - J \sim 0.7$. We have confirmed and further constrained $m_{110W} - J$ using observed spectroscopy of the same three brown dwarfs used by Luhman et al. (UGPS J072227.51–054031.2 [UGPS 0722, T9], WISE J014807.25–720258.7 [W0148, T9.5], WISE J154151.65–225024.9 [W1541, Y0.5]), and adding data for the resolved T9 and Y0 system WISEPC J121756.91+162640.2A and B (W1217A,B; Leggett et al. 2014). We find that for

the three T9 – T9.5 dwarfs $m_{110W} - J = 0.84 \pm 0.06$ and for the two Y0 – Y0.5 dwarfs $m_{110W} - J = 0.71 \pm 0.09$.¹ We exclude model spectra, given the discrepancies between observations and theory (§6). The mid-infrared properties of WD 0806–66B are similar to the Y0.5 W1541 (§4), hence we adopt $J = 25.00 \pm 0.10$ for the source.

The GMOS observations were executed via program GS-2011B-Q-53 on UT 2011 December 5, 30 and 31, and 2012 January 19, 20 and 21. Forty-five 720-second exposures at z were obtained for a total on-source time of 9 hours. Conditions were photometric with seeing around 0".8. Landolt (1992) and Smith et al. (2002) photometric standards were used for calibration each night, as is routine practice at Gemini. The data were reduced in the usual way using IRAF routines, paying particular attention to fringe correction.

The GSAOI observations were executed via program GS-2013B-Q-15. Z -band observations were obtained on UT 2013 December 17 and 18, and J -band on UT 2013 December 18 and 2014 January 15, 16 and 19. The total on-source time was 94 minutes at Z and 91 minutes at J , consisting of 120-second exposures at Z and 60-second at J . Photometric but poorer natural seeing conditions prevailed, and the adaptive optics corrected images had full-width half-maximum (FWHM) of 0".3 – 0".4. Stacking the images was difficult as there are relatively few point sources, and the FWHM of the stacked image was degraded further to $\sim 0".5$. The T9 brown dwarf UGPS 0722 and other sources near this T9 (in the 85" by 85" GSAOI field of view), were imaged on 2014 January 19, and used to determine zeropoints at Z and J and to investigate whether the GSAOI photometric system is equivalent to the Mauna Kea photometric system (MKO, Tokunaga & Vacca 2005). We also investigated the linearity behavior. We found that no linearity correction needed to be applied, and that the GSAOI Z and J filters correspond directly to the MKO Y and J . We derived identical zeropoints, within the uncertainties, for both bright and faint read modes and for each of the four detectors. The zeropoints were measured to be 26.71 at GSAOI- Z (equivalent to MKO- Y) and 26.40 at J , where zeropoint is defined as the magnitude of an object that produces one count (or data number) per second.

Figure 1 shows our Gemini images with the location of the source indicated. We used the 4.5 μm image to derive coordinates for WD 0806–66B of 8h 07m 15.195s $-66^\circ 18' 51".25$ at epoch 2009 August 24. The proper motion of the system (as determined from the white

¹We investigated trends with spectral type for $m_{110W} - Y$ but found more scatter, perhaps due to the fact that spectral type is based on the shape of the J -band flux peak, and $Y - J$ is sensitive to gravity, metallicity and cloud properties (§7). Burgasser et al. (2006) give NICMOS F110W magnitudes for a sample of T dwarfs, and those data imply $m_{110W} - J = 1.1 \pm 0.1$. However the instrument handbooks show that the system throughput of the NICMOS + F110W filter is significantly different from the WFC3 + F110W filter.

dwarf) is $0''.3403 \text{ yr}^{-1}$ in Right Ascension and $-0''.2896 \text{ yr}^{-1}$ in Declination, and the trigonometric parallax is $52.17 \pm 1.67 \text{ mas}$ (Subasavage et al. 2009). WD 0806–66B is not detected in our data, implying $z_{AB} > 26.2$, $Y > 23.5$ and $J > 23.9$, where these values correspond to the 3σ limits in the stacked z , Y and J images.

Our z and Y data extend the limits found by Luhman et al. (2014b), using archived VLT data, to fainter magnitudes. Note that our models imply that $z - J$ turns to the blue for $M_J > 18$, or T8 and later types. For early-type Y dwarfs $z - J \sim 3$ as opposed to $z - J \sim 4$ for late-type T dwarfs. Detection in the z -band of such cool objects however remains challenging, as J is intrinsically faint. Our J limit is consistent with the $J = 25.0 \pm 0.1$ implied by the $m_{110W} = 25.7 \pm 0.05$ measured by Luhman et al. Using the archived *Spitzer* data we determine $[3.6] = 19.28 \pm 0.10$ and $[4.5] = 16.78 \pm 0.05$ (slightly different from the values derived by Luhman et al. 2012). The WISE All-sky source catalog gives W2 ($4.6 \mu\text{m}$) = 17.68 ± 0.41 , W3 ($12 \mu\text{m}$) = 12.54 ± 0.16 and W4 ($22 \mu\text{m}$) = 10.18 ± 0.53 , however the W3 and W4 fluxes are much too bright, likely due to the bright infrared cirrus coincident with the source that can be seen in the WISE images.

The near-infrared magnitude limits determined here are given in Table 1. No near-infrared spectrum is available for this brown dwarf, and so a spectral type cannot be derived. For plotting purposes we assign a nominal spectral type of Y1, based on its similarity to Y0.5 – Y1 dwarfs in the color-color diagrams shown later. We compare the near- to mid-infrared colors of WD 0806–66B to model calculations in §6.

2.2. NIRI Photometry

NIRI was used on Gemini North to obtain $YJHK$ photometry, or a subset thereof, for eight T8 – Y0.5 dwarfs via programs GN-2013A-Q-63 and GN-2013B-Q-27. The photometry is on the MKO system, however there is some variation in the Y filter bandpass between the cameras used on Mauna Kea, and $Y_{\text{NIRI}} - Y_{\text{MKO}} = 0.17 \pm 0.03$ (Liu et al. 2012). Exposure times of 30 s or 60 s were used, with a 5- or 9-position telescope dither pattern. The data were reduced in the standard way using routines supplied in the IRAF Gemini package. UKIRT Faint Standards were used for calibration, taking the Y data from the UKIRT online catalog² and the JHK data from Leggett et al. (2006). All data were taken on photometric nights with typical near-infrared seeing of $0''.8$.

Table 1 gives the results, where we have applied the correction above to the Y data to

²http://www.jach.hawaii.edu/UKIRT/astrometry/calib/phot_cal/fs_ZY_MKO_wfcam.dat

get it on the standard MKO system. The date of observation is also listed. Note that the H -band measurement for W1541 is a repeat of the measurement we published in Leggett et al. (2013), and is significantly brighter — here we find $H = 21.07 \pm 0.07$ compared to the previous value of $H = 22.17 \pm 0.25$. The data used here were obtained in much better seeing, $0''.5$ compared to $0''.7$, which allowed better separation of the target from a very close star. Hence we use the results from the more recent dataset only.

2.3. FLAMINGOS-2 Photometry

FLAMINGOS-2 was used on Gemini South to obtain $YJHKs$ photometry, or a subset thereof, for eight T9 – Y1 dwarfs, via programs GS-2013B-Q-15, GS-2014A-Q-50 and GS-2014B-Q-17. In order to confirm that the photometric system corresponds to MKO for the YJH filters, and to determine the transformation from Ks to K , we observed 2MASS J04151954–0935066 (T8) and UGPS 0722 (T9) on 2013 November 22 and 27, and December 25. For the science targets, exposure times of 60 s or 120 s were used for Y , 60 s for J , and 10 s or 15 s for H and Ks , with a 5- or 9-position telescope dither pattern. The data were reduced in the standard way using routines supplied in the IRAF Gemini package. The instrument was inadvertently used in both bright and faint read mode, so zeropoints were derived for both modes. We derived zeropoints at $Y/J/H/Ks$ of 24.83/24.91/25.15/24.45 and 24.09/24.16/24.39/23.68 for bright and medium mode respectively.

The FLAMINGOS-2 Ks filter profile is very similar to that of the 2MASS Ks filter. Stephens & Leggett (2004) find that $K - Ks = 0.15$ for T8 spectral types. We determine a slightly larger correction for FLAMINGOS-2, measuring $K - Ks = 0.3$ for 2MASS 0415 and $K - Ks = 0.5 \pm 0.1$ for UGPS 0722. For all targets presented here we adopt $K - Ks = 0.4 \pm 0.1$. The YJH photometry was found to be on the MKO system, as expected from the filter bandpasses.

Table 1 gives the results, where we have applied the correction above to the Ks data to transform it to MKO K . The date of observation is also listed. The upper flux limits quoted at H and K for WISE J064723.23–623235.5 (W0647) correspond to the 3σ detection limits in each dataset.

2.4. Keck Observatory NIRC2 Archived Data

We used the Keck Observatory Archive (KOA) to access H -band imaging data for WISE J182831.08+265037.7 (W1828), taken with the NIRC2 near-infrared imager. The spectral

sub-type of W1828 is uncertain as the near-infrared spectrum of this faint object is noisy. In the literature it has been labelled as $\geq Y2$ (e.g. Beichman et al. 2014). Here we classify it as Y1.5 as it is not very different from the Y1 dwarfs in color-magnitude diagrams. Note that W1828 is more luminous than, and is therefore assumed to be earlier in type than, WISE J085510.83–071442.5 (Luhman 2014, W0855). There is no spectrum of W0855, and it has been assigned a type $> Y2$ in the literature based on the type assigned to W1828 (e.g. Tinney et al. 2014). Here we assign a nominal spectral type of Y2 to W0855 for plotting purposes (but see discussion in §4). We used NIRC2 data taken on 2011 October 16 for principal investigator Beichman. The night was photometric with excellent $0''.3$ seeing. Thirty-three frames were obtained, each consisting of a 60-second times 2-coadd exposure. A NIRC2 H -band flat was also downloaded from the KOA site. The data were reduced in the standard way using IRAF routines, and stacked using offsets measured from the images. The stacked image was calibrated using 10 sources in common with a shallower image of the field obtained using NIRC2 on 2014 July 02, via program GN-2014A-Q-64. The NIRC2 image in turn was calibrated using UKIRT photometric standards; both NIRC2 and NIRC1 use MKO H filters.

We derive $H = 22.73 \pm 0.13$ for W1828, somewhat fainter (1.6σ) than the 22.42 ± 0.14 determined by Beichman et al. (2013) from the same dataset using different secondary standards, and consistent with the 22.85 ± 0.24 measured by Kirkpatrick et al. (2012) using 2010 NIRC2 data. In this paper we adopt our measurement of $H = 22.73 \pm 0.13$.

3. Photometry Compilation and Discrepancies Between Published Magnitudes

Discrepancies between near-infrared photometry obtained at Gemini and obtained by the WISE team have been noted previously (e.g. Leggett et al. 2013). Figure 2 compares J and H magnitudes obtained by the two groups. Gemini data are taken from this work and Leggett et al. (2013); WISE team data are from Beichman et al. (2013, 2014), Kirkpatrick et al. (2012, 2013) and Mace et al. (2013). The sample consists of 14 T8 to Y1 dwarfs where we have data in common. It can be seen that for about one-third of the sample the two measurement sets differ by more than 2σ , with two J measurements differing by 6 to 7 σ . Variability in near-infrared flux has been observed for brown dwarfs. Primarily this is seen for late-L and early-T dwarfs, and has been associated with the transition from cloudy to clear atmospheres (e.g. Radigan et al. 2014). Clouds are also present in the atmospheres of late-T and Y dwarfs, however the level of variability observed for the warmer brown dwarfs is typically $\ll 10\%$, and it seems unlikely that variability can explain the large discrepancies of up to one magnitude seen here. As the scatter is larger for J than H , and there are generally

more variations in J filter bandpasses used at observatories than in H , we suspect the cause is unrecognised differences in photometric systems. These differences can be very large for objects with unusual energy distributions, such as T and Y dwarfs (e.g. 0.4 magnitudes for mid-T types, Stephens & Leggett 2004). The trends with spectral type shown in §4 support the Gemini measurements and not the WISE team results, where the two datasets disagree. Examples include the T9 0005+43 for which Mace et al. give $J - H = 0.23 \pm 0.14$ compared to our -0.39 ± 0.03 , and the T9pec 0146+42 (Dupuy et al. 2015) for which Kirkpatrick et al. (2012) and Beichman et al. give $J - H = -1.51 \pm 0.33$ compared to our -0.61 ± 0.14 .

To avoid possible systematic errors, we use only near-infrared photometry for the Y dwarfs that we are confident is on the MKO system, in this analysis. The exceptions are the recent J -band detections of WD 0806–66B (Luhman et al. 2014b) and W0855 (Faherty et al. 2014). We include these objects in order to populate the low-luminosity end of the sample. The WFC3 detection of WD 0806–66B is described in §2.1. For W0855, Faherty et al. used the FourStar imager at Las Campanas Observatory and measured $J3 = 24.8_{-0.35}^{+0.53}$, implying $J_{\text{MKO}} = 25.0_{-0.35}^{+0.53}$. We adopt the parallax given by Luhman & Esplin (2014) and assign a nominal spectral type of Y2 to this source for plotting purposes (see §2.4). Table 2 gives $YJHK$, or a subset thereof, for 17 Y dwarfs with MKO-system near-infrared photometry, together with spectral types and distance moduli as derived from published parallaxes.

For this paper, T and Y dwarf photometry is from this work, the UKIRT Infrared Deep Sky Survey (Lawrence et al. 2007), the AllWISE catalog (Wright et al. 2010, Mainzer et al. 2011), Burningham et al. (2010, 2013), Chiu et al. (2006), Dupuy et al. (2014), Faherty et al. (2014), Knapp et al. (2004), Leggett et al. (2007, 2010, 2013), Liu et al. (2011, 2012), Lucas et al. (2010), Luhman et al. (2014b), Patten et al. (2006), Pinfield et al. (2014a,b), and Wright et al. (2014). Trigonometric parallaxes for the sample are taken from the Hipparcos catalog (ESA 1997), Beichman et al. (2014), Dupuy & Kraus (2013), Luhman & Esplin (2014), Manjavacas et al. (2013), Marsh et al. (2013), Subasavage et al. (2009), Tinney et al. (2014), Vrba et al. (2004), and Wright et al. (2014).

4. Observed Trends with Spectral Type

Figure 3 shows absolute $1 - 5 \mu\text{m}$ magnitudes as a function of spectral type, and Figure 4 shows $0.9 - 12.0 \mu\text{m}$ colors as a function of type, for a sample of late-T and Y dwarfs. New data presented here are indicated by red symbols. Color sequences are better defined, as is the intrinsic scatter in the sequences, when the new data are included. The new data enable a more meaningful comparison with the models (§6).

Currently the Y dwarf spectral classification is defined by the width of the J -band flux peak in the (often noisy) near-infrared spectrum (Cushing et al. 2011, Mace et al. 2013). There are no pronounced near-infrared spectral differences between T and Y dwarfs, for the current sample of known objects. It is quite likely that as more Y dwarfs are discovered, and our understanding of their physics and chemistry improves, the late-T and Y dwarf spectral classification scheme will have to be revised (even though spectral classification should be driven by spectral features and not by physical interpretation of the atmospheres).

In the current classification scheme, T_{eff} across the T/Y boundary drops sharply — from 750 K at T8, to 600 K at T8.5, to 500 K at T9, to 400 K at Y0 (e.g. Saumon et al. 2007, Smart et al. 2010, Leggett et al. 2012 and 2013). The atmospheres are also changing dramatically, from being reasonably clear for mid-T types, to cloudy for late-T and early-Y with sulphide and chloride condensates, to cloudy with water ice for later Y types (Morley et al. 2012, 2014).

Outliers are identified in Figures 3 and 4. In the case of WISE J035000.32–565830.2 (W0350) and WISEP J140518.40+553421.4 (W1405), the brightness and color trends would be improved if their classifications were shifted 0.5 subclass later: W0350 to Y1.5 and W1405 to Y0.5. However for W0350 the absolute magnitude-color relations shown later suggest that the absolute magnitudes are also too faint, in other words the distance is too small and measured parallax too large. For one source, WISE J053516.80–750024.9 (W0535), both the near- and mid-infrared absolute magnitudes appear too bright, implying that the distance is too large (parallax too small) or the source is multiple.

W0855 is extremely red in J – $W2$, and is intrinsically fainter than any known Y dwarf, by ~ 4 magnitudes at J and ~ 2 magnitudes at $W2$ (neglecting W0350 whose parallax we suspect is erroneous). More Y dwarfs with good quality near-infrared spectra are required to establish the classification scheme beyond Y1 types. A simple extrapolation of the M_{W2} as a function of type diagram suggests a spectral type for W0855 of around Y4.

Other sources appear to have unusual spectral energy distributions. SDSS J141624.08+134826.7 (S1416B) WISE J033515.01+431045.1 (W0335) and WISE J014656.66+423410.0 (W0146) appear to be unusually faint in the K -band and blue in $J - K$ and $H - K$. S1416B is a known low-metallicity high-gravity T dwarf (e.g. Burningham et al. 2010). Similarly, Beichman et al. (2014) show that W0335 has quite a large tangential velocity, and their model interpretation suggests a relatively high gravity and an age around 8 Gyr. WISE J182831.08+265037.7 (W1828) appears unusually bright in the mid-infrared, and has been widely discussed in the literature (e.g. Beichman et al. 2013); we return to this object later in §7.4.

We also see an indication of populations with unusual $Y - J$ colors. ULAS J232600.40+020139.2 (U2326), WISE J041358.14–475039.3 (W0413) and WISE J073444.02–715744.0 (W0734) appear to be red in $Y - J$, and WISEP J173835.53+273258.9 (W1738) and W0350 appear blue in this color. We discuss $Y - J$ colors in §7.3.

5. Description of the Models

In this analysis we use spectra and colors generated from model atmospheres with a variety of cloud cover. We include cloud-free models from Saumon et al. (2012) and models with homogeneous layers of chloride and sulphide clouds from Morley et al. (2012). We also use the patchy cloud models from Morley et al. (2014), which include water clouds and have a surface that is partly clear and partly cloudy. These patchy cloud models assume a surface cloud cover fraction of 50%, and a relatively high sedimentation efficiency described by $f_{\text{sed}} = 5$, i.e. thin cloud decks. For this paper we have generated models with water clouds that have a larger surface coverage fraction of 80%, and thicker cloud decks parameterised by $f_{\text{sed}} = 3$. All of the models have solar metallicity and are for the equilibrium chemistry case, i.e. do not include vertical mixing in the atmosphere. The models have been generated for surface gravities of $\log g = 4.00, 4.48$ and 5.00 cm/s^{-2} . For a (necessarily) nearby sample of brown dwarfs with $300 < T_{\text{eff}} < 600 \text{ K}$ and expected local-neighborhood ages between 0.4 and 10 Gyr, evolutionary models show that $4 \lesssim \log g \lesssim 5$ (Saumon & Marley 2008).³

Morley et al. (2014) show that for temperatures between 300 K and 800 K, the expected dominant molecular opacity species are: CH_4 , H_2 , H_2O , NH_3 and PH_3 . The models include updated opacities for NH_3 and pressure-induced H_2 (Saumon et al. 2012). The CH_4 line list has not been updated and is known to be incomplete, however at the low temperatures of this sample the incompleteness is not expected to be severe and the effect could be modest. Figure 5 shows the opacity cross sections as a function of wavelength, extracted from the 50/50 $f_{\text{sed}} = 5$ patchy water cloud model with $T_{\text{eff}} = 400 \text{ K}$, $\log g = 4.48$ (typical of a Y0 dwarf, Leggett et al. 2014). The cross sections have been calculated for the atmosphere at the pressure and temperature of three different layers: that from which the $1 \mu\text{m}$ flux emerges, that from which the $5 \mu\text{m}$ flux emerges, and that from which the $10 \mu\text{m}$ flux emerges. The near- to mid-infrared flux emerges from layers with very different pressures and temperatures, and Figure 5 shows the dominant opacity sources for each of the three bandpasses.

³The magnitudes generated from the published models and used in this paper can be obtained at <http://www.ucolick.org/~cmorley/cmorley/Models.html>

Figure 6 shows synthetic $0.8 - 20 \mu\text{m}$ spectra for a $\log g = 4.48$ brown dwarf at 10 pc, with different cloud cover parameters and $T_{\text{eff}} = 400 \text{ K}, 300 \text{ K}$ and 250 K . These temperatures and gravity correspond to an approximately 10 Jupiter-mass object aged 3 to 10 Gyr. Far-red, near- and mid-infrared filter bandpasses are also shown in Figure 6. The water ice condensates scatter at wavelengths $\sim 1\mu\text{m}$, and absorb at $\sim 5\mu\text{m}$ (Morley et al. 2014, their Figure 2). Figure 6 shows that when the water cloud extent and depth is increased, the z and W2 fluxes are decreased, and the flux is redistributed to K , [3.6] and W3. At $T_{\text{eff}} = 400 \text{ K}$ the flux at Y and J also decreases with increasing water clouds. At $T_{\text{eff}} = 300 \text{ K}$ and 250 K very little flux emerges in the near-infrared, independent of the cloud parameters.

We compare the cloud-free and cloudy models to the observations in the next section.

6. Comparing Data to Models

Figures 7 and 8 are near- and mid-infrared color-magnitude diagrams. Figure 9 shows near-infrared colors against $J - W2$. In Figure 8, the kink in the thick water cloud model sequence at $M_{W2} \approx 16$ is due to the combination of changing opacity and pressure-temperature structure between 325 and 300 K, as water condenses into ice.

The model trends are in reasonable agreement with the data, for example Figure 7 shows that the models reproduce the redward turn in $J - H$ at $M_J \sim 21$ or $T_{\text{eff}} \sim 400 \text{ K}$. There are problematical discrepancies however, such as the divergence between models and data in $J - K$, for $M_J > 21$. Variations in gravity cannot account for the discrepancies: increasing gravity improves the match for $J - H$ but makes it worse for $J - K$, for example. Note that all models are for solar metallicity, and it is likely that the sample contains brown dwarfs with a range of metallicity. This is one area that the models still need to address.

For the $T_{\text{eff}} \leq 450 \text{ K}$ models, we find that increasing the cloud cover fraction (from 50% to 80%) and decreasing the sedimentation efficiency (from $f_{\text{sed}} = 5$ to $f_{\text{sed}} = 3$) greatly improves the agreement with most of the observed colors. To explore the validity of this change, we compare the observed near-infrared spectrum of the Y0 dwarf W1217B (Leggett et al. 2014) to $T_{\text{eff}} = 400 \text{ K}$ $\log g = 4.48$ synthetic spectra in Figure 10. Here the observed flux has been scaled to 10 pc using the trigonometric parallax measured by Dupuy & Kraus (2013), and the model fluxes are scaled to 10 pc adopting a brown dwarf radius of $0.1054 R/R_{\odot}$ based on the evolutionary models of Saumon & Morley (2008). Spectra for other Y0 dwarfs with trigonometric parallaxes are very similar in brightness, but have less complete wavelength coverage. We find that the $1.0 - 1.3 \mu\text{m}$ spectrum in fact supports very thin to no cloud, and *not* the thick cloud model.

The large photometric discrepancies (~ 1 magnitude) at $T_{\text{eff}} \approx 400$ K (spectral type Y0, $M_J \approx 20$, $M_{W2} \approx 15$) consist of the models being too blue in $J - H$, $J - K$ and W2 – W3, and too red in [3.6] – W2. Adding more extensive and thicker water clouds appears to address the problems in $J - H$, $J - K$ and W2 – W3 by reducing the flux at J , and increasing the flux at K and W3. However the spectral comparison shows that the apparent improvement is misleading — in fact the J flux becomes much too weak if the extent and thickness of the water clouds are increased. Instead, the near-infrared spectral comparison shown in Figure 10 and the photometric comparisons shown in Figures 7 — 9 indicate that the patchy cloud model fluxes for Y0 dwarfs are too low, by about a factor of two or a magnitude, at Y , H , K , [3.6] and W3. For later Y-types with $T_{\text{eff}} \approx 300$ K, additional discrepancies seem to arise.

We discuss possible solutions to these problems in the next section.

7. Discussion

7.1. Y0 Dwarfs, $T_{\text{eff}} \approx 400$ K

As noted above, for Y0 dwarfs with $T_{\text{eff}} \approx 400$ K, we have found that our state-of-the-art models generate fluxes that are about a factor of two too low at Y , H , K , [3.6] and W3 (filter profiles are shown in Figure 6). For the Y , H and W3 bandpasses (the ~ 1.05 , 1.6 and 12.0 μm spectral regions) Figure 5 shows that the dominant opacity source is NH_3 . Figure 5 also includes cross sections for an arbitrary reduction in NH_3 abundance of a factor of two. In that case the dominant opacity in the Y -band and in the blue wing of the H -band (1.5 – 1.6 μm) becomes pressure-induced H_2 . The result would be that the pronounced double absorption feature at 1.03 μm goes away, and the flux in the Y and H -bands significantly increases, all of which is in agreement with the observations (see Figure 10). Note that the dominant opacity in the J -band is already H_2 , and the agreement between the cloud-free or thin-cloud models and the data are good for J (Figure 10).

For most of the W3 band (8 – 17 μm) the dominant opacity is NH_3 and remains so even if the abundance is halved. However the absorption would be dramatically weakened – note that Figure 5 is plotted on a log scale. In this band, weakening the NH_3 absorption could mimic the gain caused by the redistribution of flux due to increasing cloud cover (Figure 6).

With ammonia absorption significantly reduced, the remaining problems would be too little flux in the K - and [3.6]-bands. The 2 – 4 μm flux is sensitive to CH_4 opacity (Figure 5) and new models should be calculated with a more complete CH_4 linelist (although, as mentioned previously, at these very low temperatures large changes are not expected). The

pressure-temperature structure of new models will in any case change once the change in the NH_3 absorption is incorporated, and this alone is likely to impact the $2 - 4 \mu\text{m}$ flux.

For higher T_{eff} models than considered here, convective mixing leads to more N_2 and less NH_3 in the spectrum-forming part of the atmosphere (e.g. at $T_{\text{eff}} \approx 600 \text{ K}$, Leggett et al. 2009). However Morley et al. (2014, their Figure 16) show that preliminary models which include vertical mixing do not resolve the discrepancies for 400 K brown dwarfs — the introduction of disequilibrium chemistry has a large impact on the $H - K$ color in particular, and makes the disagreement between models and data worse. These atmospheres are extremely complex, with low-lying chloride and sulphide clouds, high water clouds and possibly multiple convective zones (Morley et al. 2014, their Figure 4). Including vertical mixing in this context in a consistent fashion is challenging. The next stage in model generation will likely require an inversion approach, where a retrieval algorithm iterates both the pressure-temperature profile and the abundances to find the best match to the data (Line et al. 2014).

7.2. Y1 Dwarfs, $T_{\text{eff}} \approx 350 \text{ K}$

For brown dwarfs with $M_J \gtrsim 22$ and $T_{\text{eff}} \approx 350 \text{ K}$, additional issues with the models appear. The discrepancy at $J - H$ and $J - K$ increases by around 0.5 magnitudes (Figure 7). In the mid-infrared it appears that $M_{\text{W}2}$ increases more slowly with $J - \text{W}2$ than calculated (Figure 8). These could point to a significant reduction of the $1 \mu\text{m}$ flux, of about a factor of two, so that $J - H$, $J - K$ and $J - \text{W}2$ become much redder.

At $T_{\text{eff}} \approx 350 \text{ K}$ thick water clouds may be required to reproduce the data, as Figure 10 shows that such clouds cause a drop in the $1 \mu\text{m}$ flux of about the required size. Also the thick water cloud sequences in Figure 8 show interesting trends at $300 \lesssim T_{\text{eff}} \text{ K} \lesssim 350$ which are similar to those observed. The thick water cloud model has a shoulder in the trend of increasing $M_{\text{W}2}$ with increasing $J - \text{W}2$, followed by a sharp drop in $M_{\text{W}2}$. This flattening of the decrease in $M_{\text{W}2}$ followed by a dramatic drop could explain both the brightness of W1828 *and* the faintness of W0855, in W2 ($5 \mu\text{m}$; see §7.4).

Figure 11 reproduces the $J - \text{W}2 : M_{\text{W}2}$ diagram. A simple solution to the apparent brightness of W1828 is that it is an equal-mass binary (see discussion in §7.4). Making this assumption, we have fit a polynomial to the observed $J - \text{W}2 : M_{\text{W}2}$ data, weighted by the inverse of the square of the uncertainty in the absolute magnitude, excluding known binaries. We find that the fifth-order polynomial

$$M_{\text{W}2} = 8.93387 + 4.37546 * x - 1.80318 * x^2 + 0.376357 * x^3 - 0.0359539 * x^4 + 0.00126562 * x^5$$

reproduces the trend seen in the observed data with W1828 as an equal-mass binary (Figure 11). The polynomial fit is not scientifically significant and we have not derived any measures of quality of fit. We would expect the sample to have a range in metallicity, gravity and cloud properties which would result in scatter in the $J - W2 : M_{W2}$ diagram (see §7.3). The function is useful, however, as a reference for future observations and theoretical modelling. The function does show similarity to the thick water cloud model sequence in Figure 8, which gives some support to its validity. If that model sequence is shifted to fainter J and brighter $W2$ magnitudes, say $J + 1$ and $W2 - 0.3$, then there would be a shoulder at $M_{W2} \sim 15.5$, followed by rapidly increasing $W2$ for $J - W2 \gtrsim 9$, as seen in Figure 11.

Water ice scatters at J and absorbs at $W2$, and so these colors likely constrain the ice particle size and composition, as well as cloud cover. Clearly this is a very interesting and challenging parameter space for atmospheric modeling. An inversion approach may also be necessary to improve the models at these temperatures. Note that for $T_{\text{eff}} < 300$ K vertical transport no longer affects the NH_3 abundance because it is far more abundant than N_2 down to deep levels in the atmosphere.

7.3. Intrinsic Scatter

There is a large range, of about one magnitude, in the observed $Y - J$ and $J - K$ colors for $T_{\text{eff}} \sim 400$ K (Figures 7 and 9). The models in this temperature range show that Y , J and K are sensitive to the details of the cloud structure (Figures 6 and 10). Also, we have shown that the NH_3 absorption is likely to be much lower than calculated, implying that pressure-induced H_2 becomes an important opacity source at $1.55 \mu\text{m}$ and dominant at 1.05 , 1.25 and $2.05 \mu\text{m}$ (Figure 5). These wavelength regions coincide with the $YJHK$ filter bandpasses which were designed to avoid the Earth’s H_2O absorption bands. The observed near-infrared colors will become a function of the H_2 absorption, which in turn is dependent on metallicity and gravity (Saumon et al. 2012). The spread in the near-infrared colors for spectral types around Y0 therefore likely reflects a range of metallicity, gravity and cloud properties.

7.4. WISEP J182831.08+265037.8 and WISE J085510.83–071442.5

Of the known Y dwarfs, the reddest in $J - W2$ are W1828 (Y1.5) and W0855 (nominally Y2). These are likely to be the coolest of the known Y dwarfs.

W1828 appears unusually bright in the mid-infrared, and has been widely discussed in

the literature (Beichman et al. 2013 and references therein). The WISE atlas image does not show any obvious infrared cirrus coincident with the source, which might lead to a mid-infrared excess. This work and other recent publications have produced more photometry and parallaxes for comparable objects, and we can explore the nature of W1828 further.

We have calculated the colors of a binary system composed of W0647 (Y1) and W0855. A simple composite of these two sources put at the same distance does not produce a binary that is sufficiently red in J –W2 however. This is because W0855 is intrinsically faint and does not contribute enough to the mid-infrared total flux. Instead, as mentioned in §7.2, we suggest that W1828 is a simple pair of identical brown dwarfs. Each component would have $M_J \approx 24.4$ and $M_{W2} \approx 15.2$. Such a source has colors consistent with the trends seen in Figures 7 to 9. Binaries are not uncommon in brown dwarf samples — Radigan et al. (2013) find a volume-corrected binary fraction for L9 to T4 types of $13^{+7}_{-6}\%$, similar to values reported for other brown dwarf spectral types. Also, Burgasser et al. (2007) find that very low mass multiple systems tend to be closely separated and are more frequently in near-equal mass configurations.

The binary explanation of W1828 would imply that it consists of a pair of $300 \lesssim T_{\text{eff}} \text{ K} \lesssim 350$ brown dwarfs. For W0855, our models together with the observed J - and W2-band luminosity imply that it is a ~ 250 K dwarf. If W1828 and W0855 are say 3 Gyrs old (being in the solar neighbourhood), evolutionary models show that their masses are ~ 10 and ~ 5 Jupiter-masses respectively (Saumon & Marley 2008).

8. Conclusion

We have found that current state-of-the-art models can qualitatively reproduce the trends seen in the observed colors of the latest-type T dwarfs and known Y dwarfs. However significant discrepancies exist. For brown dwarfs with $T_{\text{eff}} \approx 400$ K, corresponding to spectral type $\sim Y0$, the model fluxes are a factor of two low at Y , H , K , $[3.6]$ and W3. For $T_{\text{eff}} \approx 350$ K, corresponding to spectral type $\sim Y1$, it appears that a reduction in the J -band flux of about a factor of two is needed, while the W2 flux remains approximately constant.

The problems at Y , H and W3 (or ~ 1.05 , 1.6 and $12.0 \mu\text{m}$) may be addressed by significantly reducing the NH_3 absorption, for example by halving the abundance of NH_3 . This could be explained by mixing of N_2 and NH_3 , as is seen in T dwarfs, but incorporating mixing in a realistic way in an atmosphere with chloride, sulfide and water condensates is challenging. Once the NH_3 absorption is reduced, pressure-induced H_2 becomes the dominant opacity source in the near-infrared filter bandpasses, making those colors sensitive to gravity

and metallicity variations, and probably explaining the scatter seen in the near-infrared colors of Y0 dwarfs.

While the cloud layers are thin to non-existent for the 400 K brown dwarfs, as T_{eff} decreases to 350 K thick and extensive water clouds appear to form, based on the observed reduction in the J -band flux. The onset of these clouds might occur over a narrow range of T_{eff} , as indicated by the observed small change in $5 \mu\text{m}$ flux over a large change in $J - W2$ color.

Diagnosis of cloud cover for Y dwarfs however will remain uncertain until the models, which are already complex, can be further improved to the point of reproducing the near- and mid-infrared observations. The expectation had been that the atmospheres of the cold brown dwarfs would be simpler, because most elements are condensed out and the chemistry is reduced to CH_4 , H_2O and NH_3 , but this was clearly rather optimistic.

DS is supported by NASA Origins NNH12AT89I. Based on observations obtained at the Gemini Observatory, which is operated by the Association of Universities for Research in Astronomy, Inc., under a cooperative agreement with the NSF on behalf of the Gemini partnership: the National Science Foundation (United States), the Science and Technology Facilities Council (United Kingdom), the National Research Council (Canada), CONICYT (Chile), the Australian Research Council (Australia), Ministério da Ciência, Tecnologia e Inovação (Brazil) and Ministerio de Ciencia, Tecnología e Innovación Productiva (Argentina). SKL's research is supported by Gemini Observatory. This publication makes use of data products from the Wide-field Infrared Survey Explorer, which is a joint project of the University of California, Los Angeles, and the Jet Propulsion Laboratory/California Institute of Technology, funded by the National Aeronautics and Space Administration. This research has made use of the NASA/ IPAC Infrared Science Archive, which is operated by the Jet Propulsion Laboratory, California Institute of Technology, under contract with the National Aeronautics and Space Administration. This research has made use of the Keck Observatory Archive (KOA), which is operated by the W. M. Keck Observatory and the NASA Exoplanet Science Institute (NExScI), under contract with the National Aeronautics and Space Administration.

REFERENCES

- Beichman, C. et al. 2013, ApJ, 764, 101
Beichman, C. et al. 2014, ApJ, 783, 68

- Burgasser, A. J. et al. 1999, ApJ, 522, L65
- Burgasser, A. J. et al. 2006, ApJS, 166, 585
- Burgasser, A. J., Reid, I. N., Siegler, N., Close, L., Allen, P., Lowrance, P. & Gizis, J. 2007, Protostars and Planets V, B. Reipurth, D. Jewitt, and K. Keil (eds.), University of Arizona Press, Tucson, 951, 427
- Burningham, B. et al. 2010, MNRAS, 406, 1885
- Burningham, B. et al. 2013, MNRAS, 433, 457
- Carrasco E. R. et al. 2012, Proc. SPIE 8447, Adaptive Optics System III, 84470N
- Chiu, K., Fan, X., Leggett, S. K., Golimowski, D. A., Zheng, W., Geballe, T. R., Schneider, D. P. & Brinkmann, J., 2006, AJ, 131, 2722
- Cushing, M. C. et al. 2011, ApJ, 743, 50
- Dupuy, T. J. & Kraus, A. L. 2013, Science, 341, 1492
- Dupuy T. J., Liu, M. C. & Leggett, S. K. 2015, in preparation
- Eikenberry, S. et al. 2004, SPIE 5492, 1196
- ESA 1997, The Hipparcos and Tycho Catalogues (ESA SP-1200) (Noordwijk: ESA)
- Faherty, J. K., Tinney, C. G., Skemer, A. & Monson, A. J. 2014, ApJ, 793, L16
- Hodapp, K. W. et al. 2003, PASP, 115, 1388
- Hook, I. et al. 2004, PASP, 116, 425
- Kirkpatrick, J.D. et al. 2011, ApJS, 197, 19
- Kirkpatrick, J. D. et al. 2012, ApJ, 753, 156
- Kirkpatrick, J.D. et al. 2013, ApJ776, 128
- Knapp, G.R. et al. 2004, AJ, 127, 3553
- Landolt 1992, AJ, 104, 340
- Lawrence, A. et al. 2007, MNRAS, 379,1599
- Leggett, S. K. et al. 2002, ApJ,564,452

- Leggett, S. K. et al. 2006, MNRAS, 373, 781
- Leggett, S. K. et al. 2007, ApJ, 655, 1079
- Leggett, S. K. et al. 2009, ApJ, 695, 1517
- Leggett, S. K. et al. 2010, ApJ, 710, 1627
- Leggett, S. K. et al. 2012, ApJ, 748, 74
- Leggett, S. K. et al. 2013, ApJ, 763, 130
- Leggett, S. K., Liu, M. C., Dupuy, T. J., Morley, C. V., Marely, M. S. & Saumon, D. 2014, ApJ, 780, 62
- Line, M. R., Fortney, J., Marley, M. S. & Sorahana, S. 2014, ApJ, 793, 33
- Lissauer J. L. et al. 2011, Nature, 470, 53
- Liu, M. C. et al. 2011, ApJ, 740, 108
- Liu, M. C., Dupuy, T. J., Bowler, B. P., Leggett, S. K. & Best, W. M. J. 2012, ApJ, 758, 57
- Liu, M. C. et al. 2013, ApJ, 777, L20
- Lucas, P. W. et al. 2010, MNRAS, 408, L56
- Luhman, K. L., Burgasser, A. J. & Bochanski, J. J. 2011, ApJ, 730, L9
- Luhman, K. L. et al. 2012, ApJ, 744, 135
- Luhman, K. L. 2014, ApJ, 786, L18
- Luhman, K. L. & Esplin, T. L. 2014, ApJ, 796, 6
- Luhman, K. L., Morley, C. V., Burgasser, A. J., Esplin, T. L. & Bochanski, J. J. 2014, ApJ, 794, 16
- Mace G. N. et al. 2013, ApJS, 205, 6
- Mainzer, A. et al. 2011, ApJ, 731, 53
- Marsh K. A. et al. 2013, ApJ, 762, 119
- Manjavacas E., Goldman, B, Reffert, S. & Henning, T. 2013, A&A, 560, 52

- Mayor M. & Queloz, D. 1995, *Nature*, 378, 355
- McGregor P. et al. 2004, *Proc. SPIE*, 5492, Ground-based Instrumentation for Astronomy, 1033
- Morley, C. V., Fortney, J. J., Marley, M. S., Visscher, C., Saumon, D. & Leggett, S. K. 2012, *ApJ*, 756, 172
- Morley, C. V., Marley, M. S., Fortney, J. J., Lupu, R., Saumon, D., Greene, T. & Lodders, K. 2014, *ApJ*, 787, 78
- Nakajima, T., Oppenheimer, B. R., Kulkarni, S. R., Golimowski, D. A., Matthews, K. & Durrance, S. T. 1995, *Nature*, 378, 463
- Patten, B.M. et al. 2006, *ApJ*, 651, 502
- Pinfield, D. J. et al. 2014a, *MNRAS*, 437, 1009
- Pinfield, D. J. et al. 2014b, *MNRAS*, 444, 1931
- Radigan, J., Jayawardhana, R., Lafreniere, D., Dupuy, T., Liu, M. C. Scholz, A. 2013, *ApJ*, 778, 36
- Radigan, J., Lafreniere, D., Jayawardhana, R. & Artigau, E. 2014, *ApJ*, 793, 75
- Rodriguez, D. R., Zuckerman, B., Melis, C. & Song, I. 2011, *ApJ*, 732, L29
- Saumon D. et al. 2007, *ApJ*, 656, 1136
- Saumon, D. & Marley, M. S. 2008, *ApJ*, 689, 1327
- Saumon D. et al. 2012, *ApJ*, 750, 74
- Smart, R. L. et al. 2010, *A&A*, 511, 30
- Smith J. A. et al. 2002, *AJ*, 123, 2121
- Stephens D. S. et al. 2009, *ApJ*, 702, 154
- Strauss M. et al. 1999, *ApJ*, 522, L61
- Subasavage J.P. et al. 2009, *AJ*, 137, 4547
- Tinney C. G., Faherty, J. K., Kirkpatrick, J. D., Cushing, M., Morley, C. V. & Wright, E. L. 2014, *ApJ*, in press

Tokunaga, A. T. & Vacca, W. D. 2005, *PASP*, 117, 421

Vrba, F.J. et al. 2004, *AJ*, 127, 2948

Wright, E. L. et al. 2010, *AJ*, 140, 1868

Wright, E. L. et al. 2014, *AJ*, 148, 82

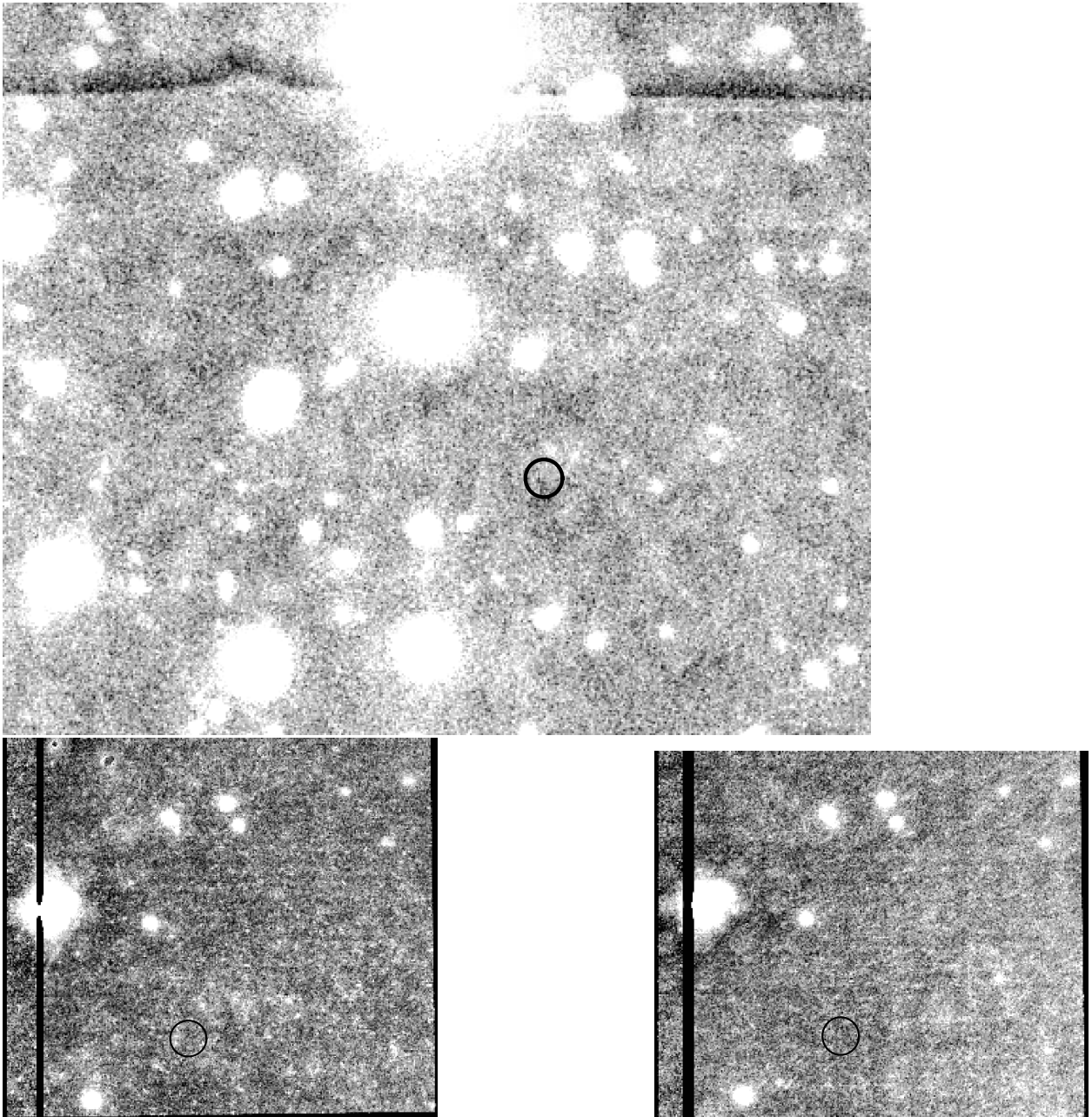


Fig. 1.— Images of the field around WD 0806–66B. The top panel is our coadded GMOS z image, with North up and East to the left, approximately 1 arcminute on a side. The lower two panels are our GSAOI images, Z -band on left (equivalent to MKO Y) and J -band on right. The images are approximately 25 arcseconds on a side. The expected location of the brown dwarf is shown as a black circle.

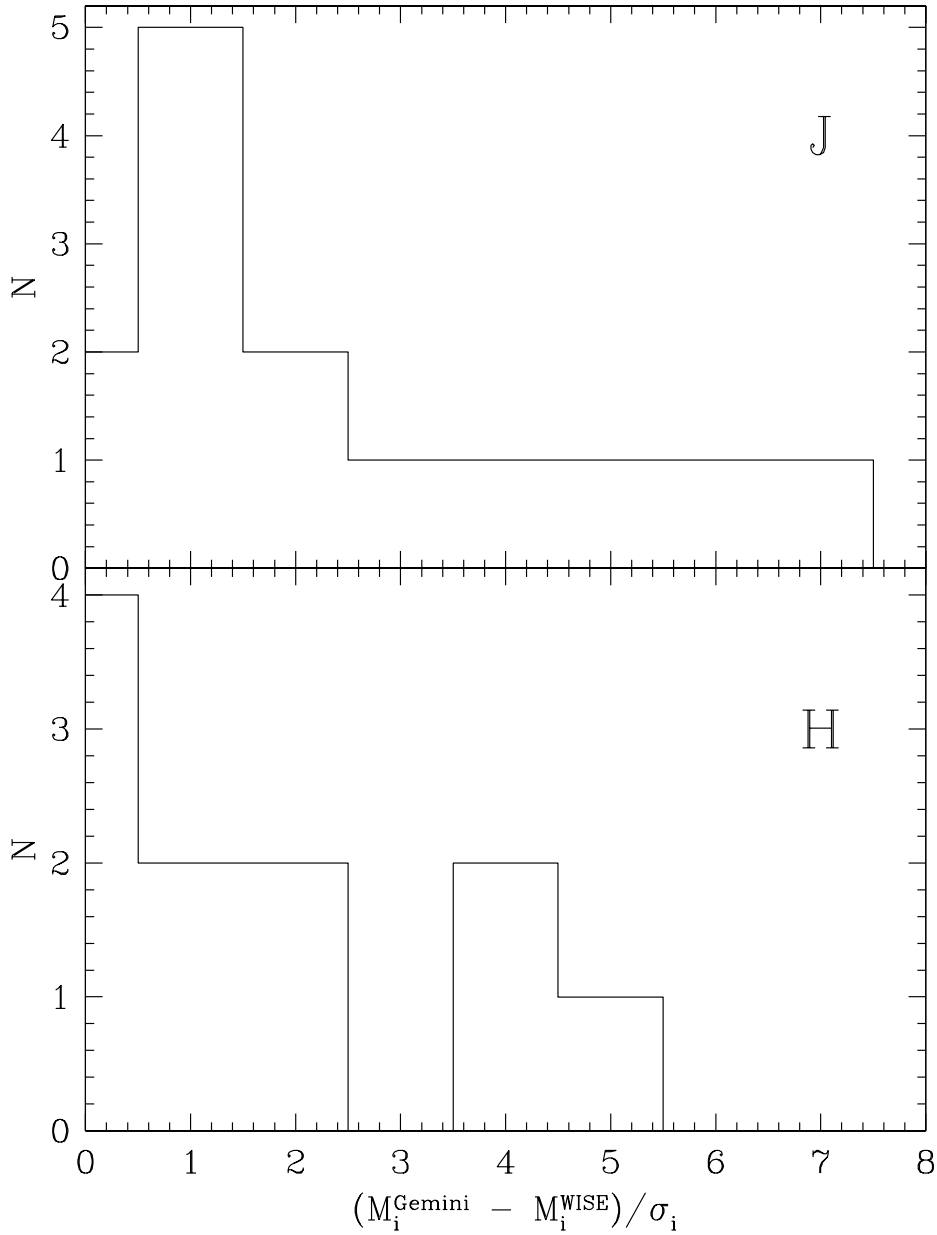


Fig. 2.— A comparison of the J and H magnitudes published by our group (this work and Leggett et al. 2013) and the WISE group (Beichman et al. 2013, 2014; Kirkpatrick et al. 2012, 2013; Mace et al. 2013). The bins show the difference between the measured values from each group divided by the square root of the sum of the squares of the uncertainties quoted for each measurement. About one-third of the sample have measurements that differ by more than 2σ .

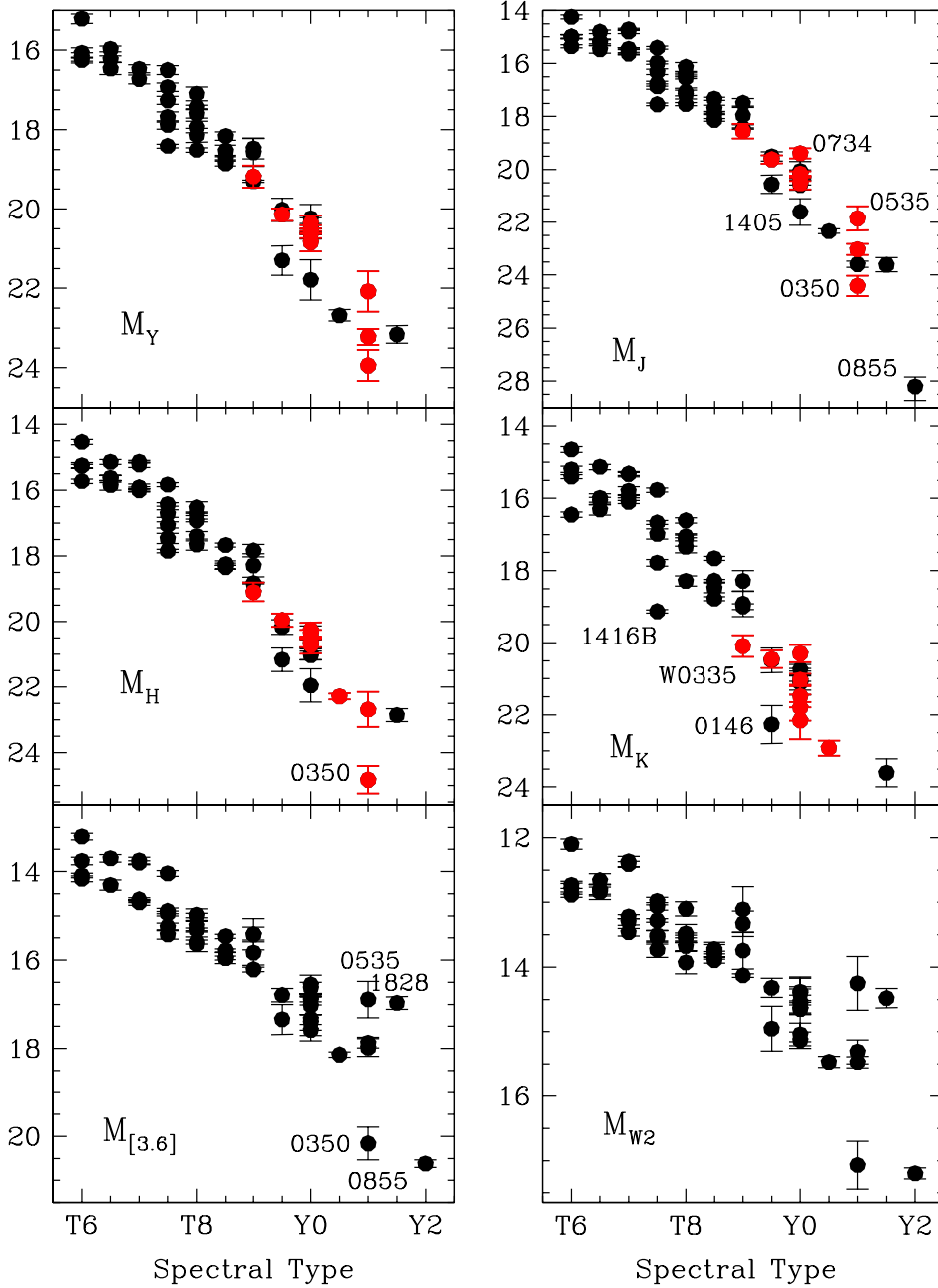


Fig. 3.— Trends in absolute magnitude as a function of spectral type. Note the varied y-axis ranges. All magnitudes are Vega based. The $YJHK$ are on the MKO system, [3.6] on the *Spitzer* IRAC system and W2 ($4.6 \mu\text{m}$) on the *WISE* system. Photometry and parallax sources are given in the text. New observations presented here are identified by red symbols.

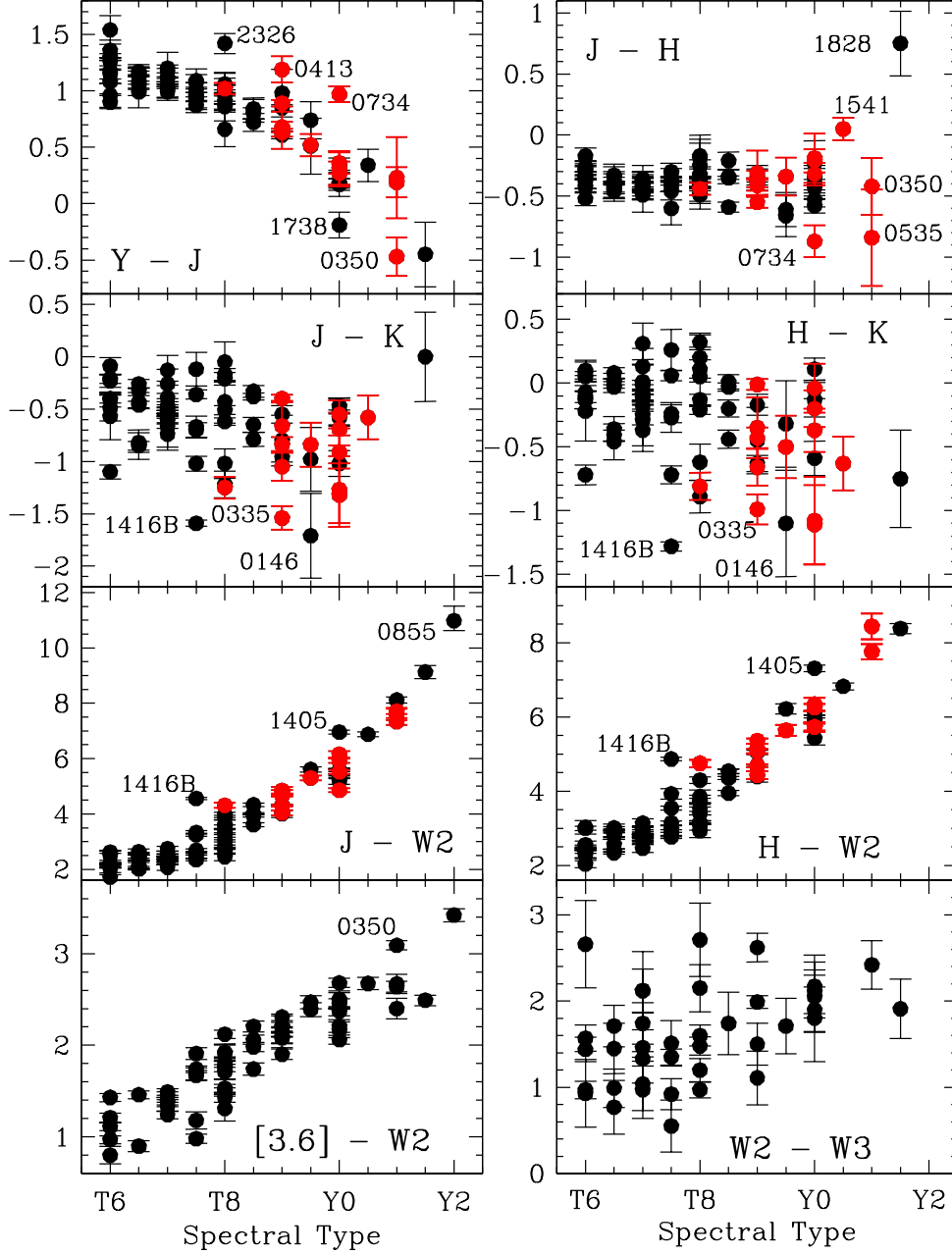


Fig. 4.— Trends in color as a function of type. Data sources are given in the text. All magnitudes are Vega based. New observations presented here are identified by red symbols.

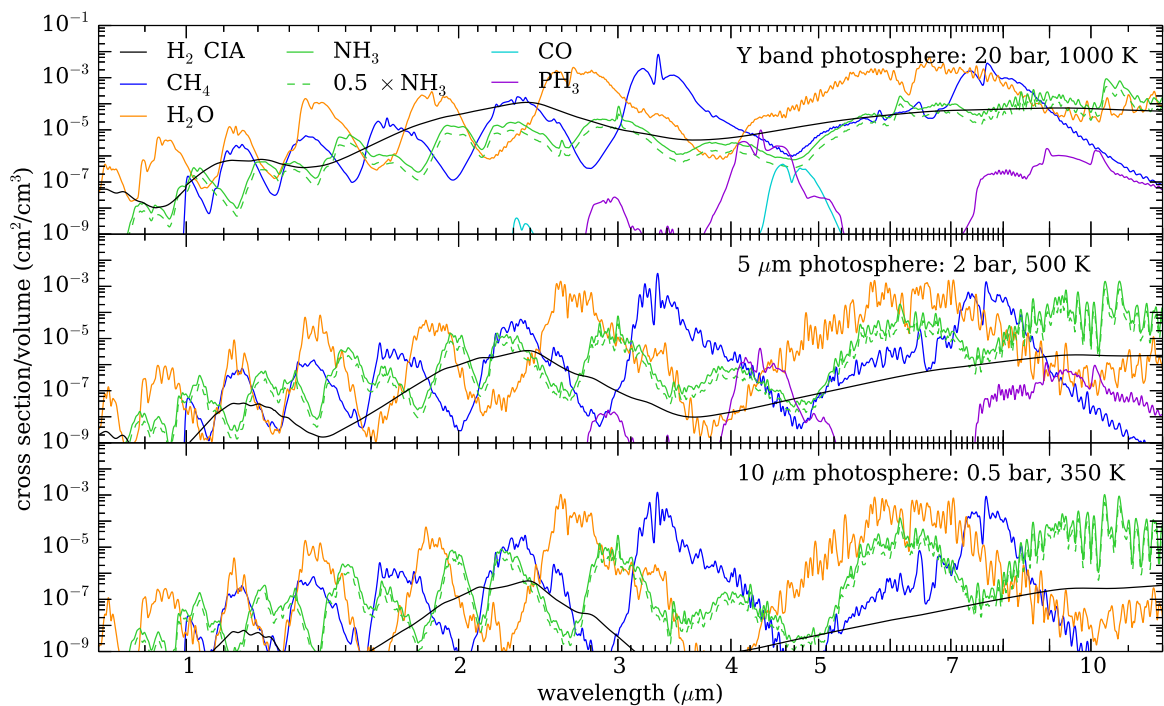


Fig. 5.— Opacity cross sections multiplied by equilibrium gas volume mixing ratio, calculated for three layers of a $T_{\text{eff}} = 400$ K, $\log g = 4.48$, brown dwarf atmosphere. The top panel shows the layer from which the Y-band flux emerges, the middle panel the $5 \mu\text{m}$ flux, and the bottom panel the $10 \mu\text{m}$ flux. See text for discussion.

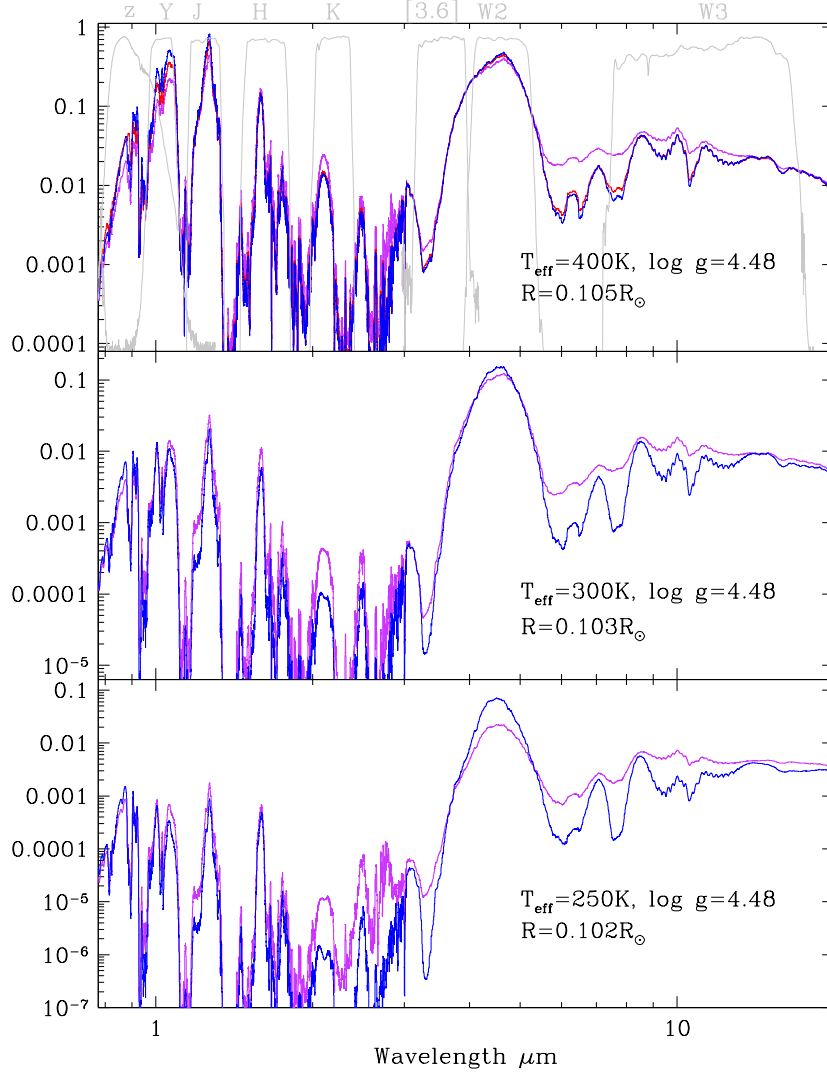


Fig. 6.— Blue, violet and red lines are synthetic spectra for a $\log g = 4.48$ brown dwarf at 10 pc. Spectra for three values of T_{eff} are shown, as indicated in the legend. The radii given by evolutionary models (Saumon & Marley 2008), and used to scale the model fluxes, are also given in the legend. Flux is plotted as F_{λ} in units of $10^{-16} \text{ W m}^{-2} \mu\text{m}^{-1}$. The red line has thin water cloud decks with $f_{\text{sed}} = 5$ over half the surface, and the violet line has thick water cloud decks with $f_{\text{sed}} = 3$ over 80% of the surface. The blue line is for a cloud-free atmosphere. Gray lines in the top panel show photometric filter bandpasses as identified by the legend: z , Y , J , H , K , *Spitzer* [3.6], and *WISE* W2 ($4.6 \mu\text{m}$) and W3 ($12 \mu\text{m}$).

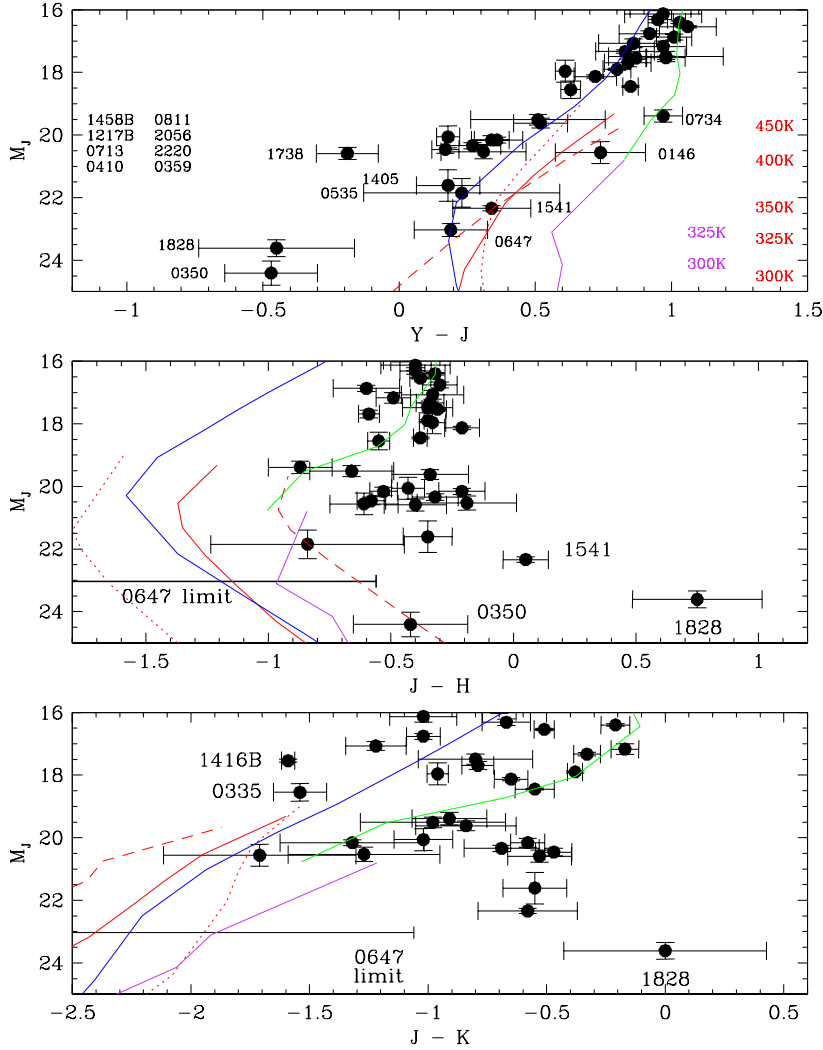


Fig. 7.— Absolute J magnitude as a function of near-infrared colors for T8 and later type dwarfs. Not shown are WD 0806–66B with $M_J = 23.6$, $z_{\text{AB}} - J > 1.2$ and $Y - J > -1.5$, and WISE J085510.83–071442.5 with $M_J \approx 28.3$ (see §2). WISE J035000.32–565830.2 appears unusually faint in M_J (and M_{W2}) and the parallax should be confirmed. Model sequences (Saumon et al. 2012, Morley et al. 2012, 2014) are shown for $\log g = 4.48$: blue lines are cloud-free, green have thin sulfide and salt cloud decks with $f_{\text{sed}} = 5$ over the entire surface, red have thin water cloud decks with $f_{\text{sed}} = 5$ over half the surface, and violet have thick water cloud decks with $f_{\text{sed}} = 3$ over 80% of the surface. The dashed line is for $\log g = 5.0$ and dotted for $\log g = 4.0$. The right axis of the top panel shows T_{eff} values for the $\log g = 4.48$ water cloud models.

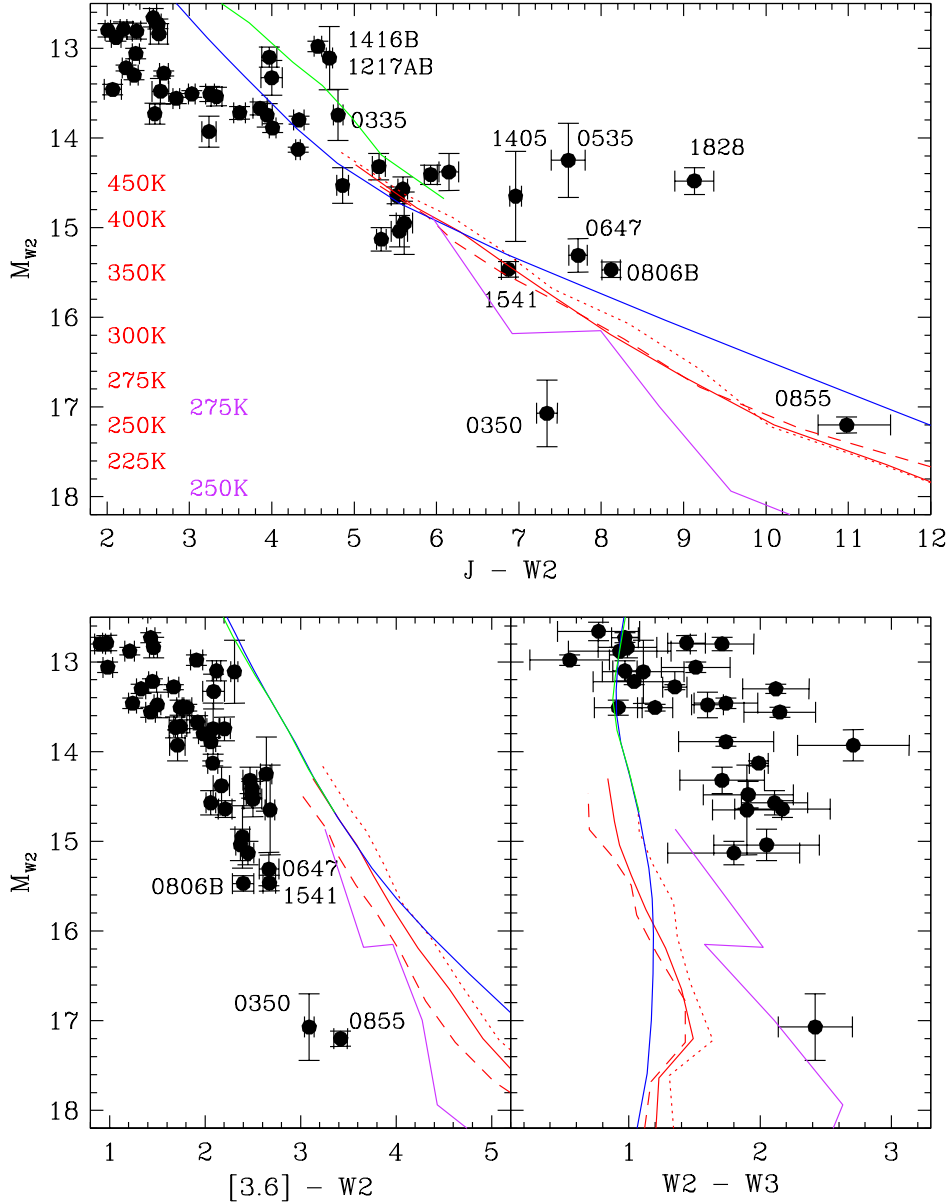


Fig. 8.— Absolute W2 magnitude as a function of various colors for T7 and later type dwarfs. For WD 0806–66B the W2 magnitude is uncertain ($\delta M = 0.4$) and we have replaced it with the *Spitzer* 4.48 μm magnitude transformed to W2 by adding 0.1 magnitude (Leggett et al. 2013). See note regarding WISE J035000.32–565830.2 in the caption to Figure 7. Sequences are as in Figure 7.

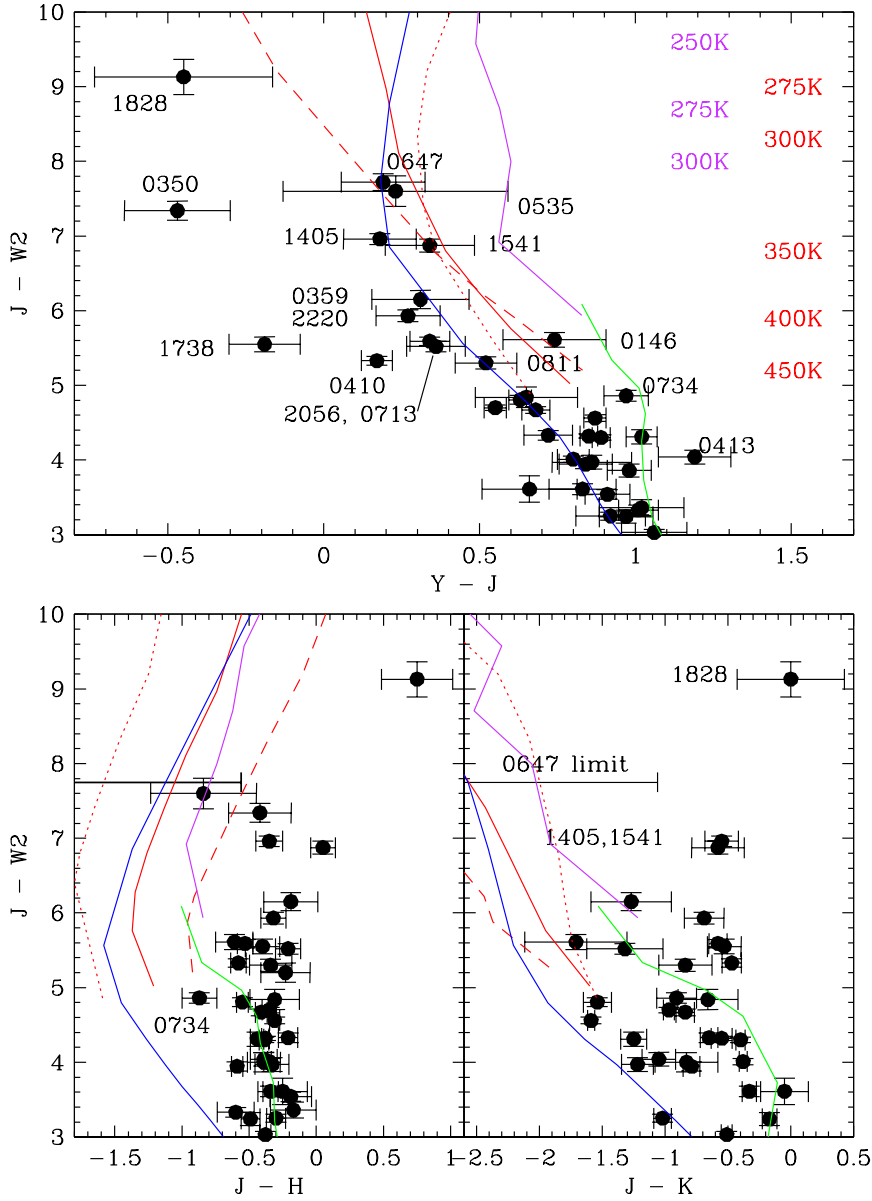


Fig. 9.— $J - W2$ as a function of color. Not shown are WD 0806–66B ($J - W2 = 8.1$) and W0855 ($J - W2 \approx 11.0$), neither of which have measured Y , H or K values available. Sequences are as in Figure 7.

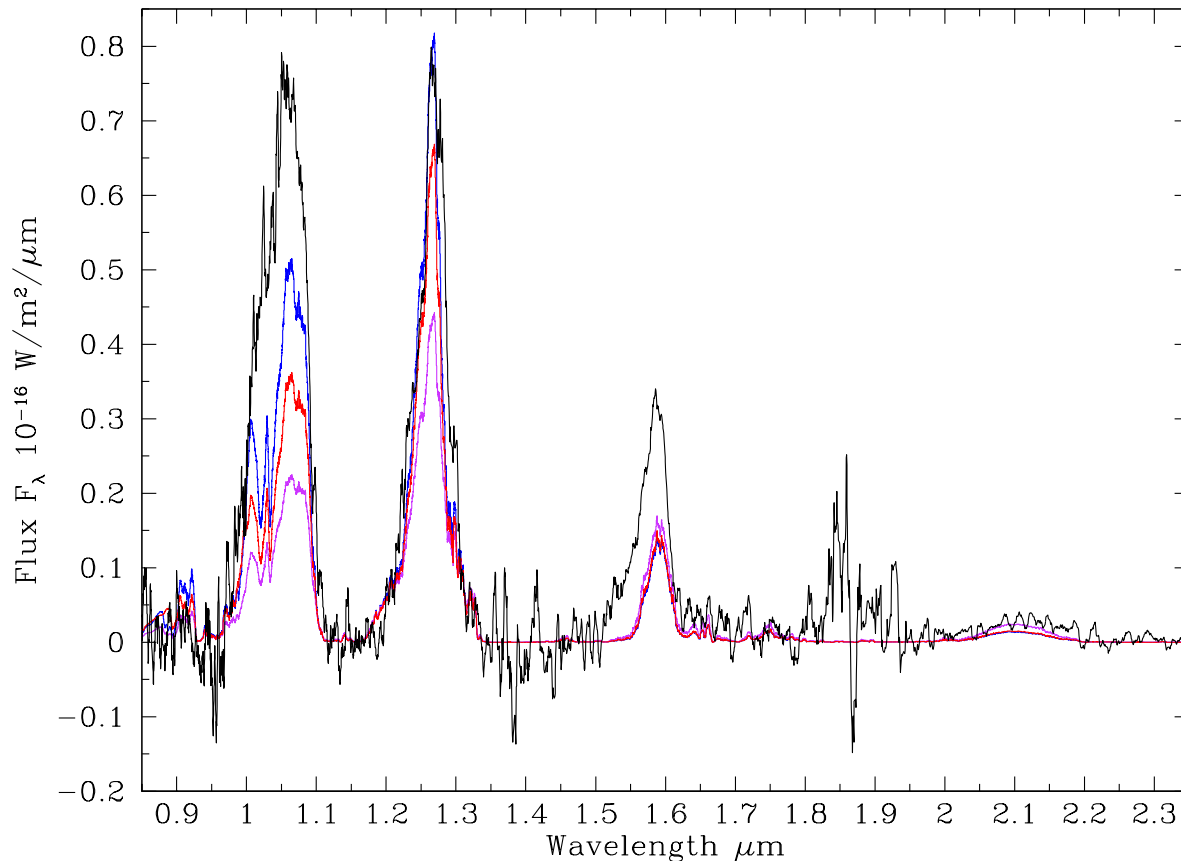


Fig. 10.— The observed (smoothed) near-infrared spectrum for the Y0 WISEPC J121756.91+162640.2B (Leggett et al. 2014) is shown as a black line. The flux has been scaled to what would be observed were the dwarf at a distance of 10 pc. The region of poor atmospheric transmission 1.80 – 1.94 μm is noisy. The blue, red and violet lines are synthetic spectra for a $T_{\text{eff}} = 400$ K $\log g = 4.48$ brown dwarf at 10 pc, with different cloud cover parameters as in Figure 7.

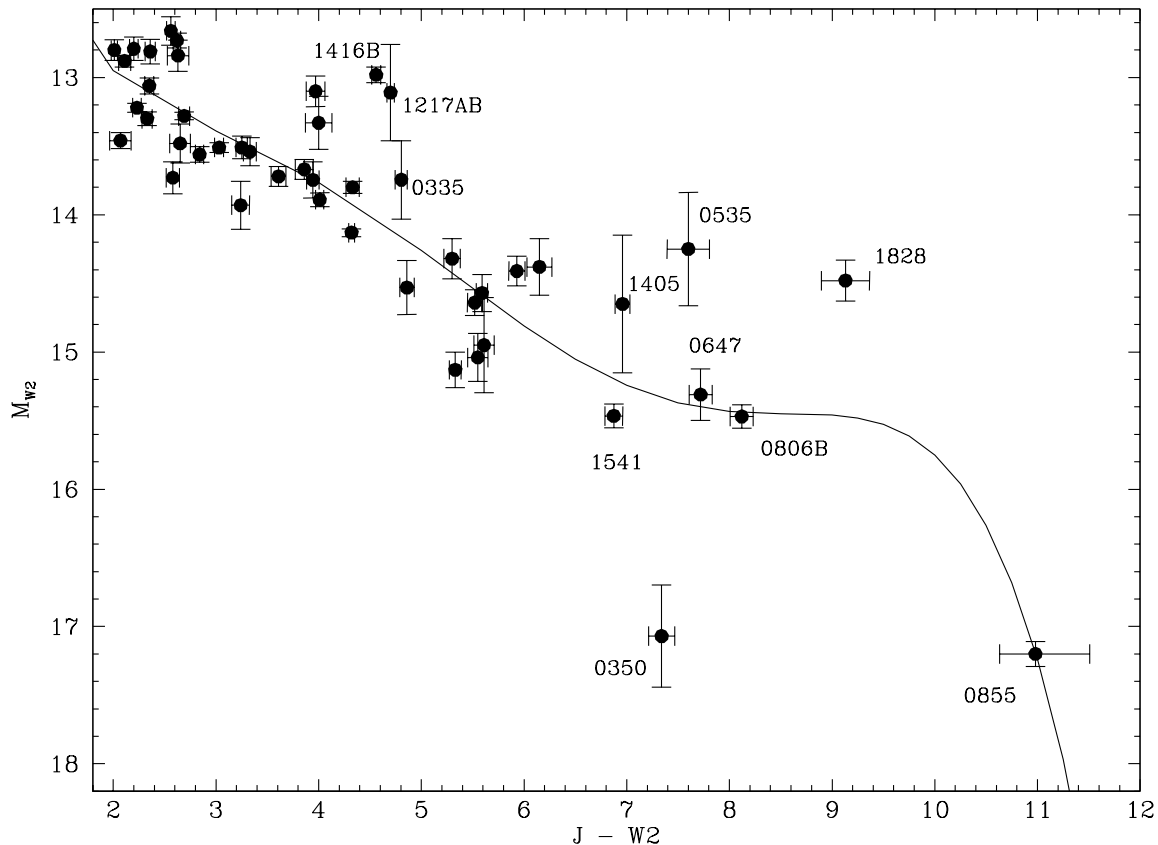


Fig. 11.— The black line is fifth-order polynomial weighted fit to the $J - W2$, M_{W2} data points, excluding known binaries. The fit is not scientifically significant, and is intended only as an indication of observed trends, with the assumption that W1828 is an equal-mass binary. W0350 is included in the fit, however the parallax for this object appears to be erroneous. While admittedly arbitrary, we note that a very similar trend can be obtained by shifting the thick water cloud model sequence in $J - W2$ and M_{W2} (Figure 8, violet line).

Table 1. New *YJHK* MKO Photometry

Name	Spectral Type	<i>Y</i> (err) ^a	<i>J</i> (err)	<i>H</i> (err)	<i>K</i> (err) ^a	Date YYYYMMDD	Instrument	Discovery Reference
WISE J000517.48+373720.5	T9	18.48(0.02)	17.59(0.02)	17.98(0.02)	17.99(0.02)	2013 0717	NIRI	M13
WISE J001354.39+063448.2	T8	20.56(0.04)	19.54(0.03)	19.98(0.04)	20.79(0.10)	2013 0812	NIRI	P14a
WISE J033515.01+431045.1	T9	19.95(0.03)	19.32(0.02)	19.87(0.04)	20.86(0.11)	2013 1127	NIRI	K12
WISE J035000.32−565830.2	Y1	21.62(0.12)	22.09(0.12)	22.51(0.20)	...	2014 0104,0108,1008,1104	FLAMINGOS-2	K12
WISE J035934.06−540154.6	Y0	21.84(0.11)	21.53(0.11)	21.72(0.17)	22.8(0.3)	2013 1121,1122	FLAMINGOS-2	K12
WISE J041358.14−475039.3	T9	20.82(0.10)	19.63(0.06)	20.02(0.08)	20.68(0.12)	2013 1121	FLAMINGOS-2	M13
WISE J053516.80−750024.9	Y1	22.73(0.30)	22.50(0.20)	23.34(0.34)	...	2014 0105,0106,1008	FLAMINGOS-2	K12
WISE J064723.23−623235.5 ^b	Y1	23.13(0.09)	22.94(0.10)	> 23.5	> 24	2014 0111,0220,0222,0223	FLAMINGOS-2	K13
WISE J071322.55−291751.9	Y0	20.34(0.08)	19.98(0.05)	20.19(0.08)	21.30(0.31)	2013 0112	NIRI	K12
WISE J073444.02−715744.0	Y0	21.02(0.05)	20.05(0.05)	20.92(0.12)	20.96(0.15)	2013 1127	FLAMINGOS-2	K12
WISEPA J075108.79−763449.6	T9	20.02(0.10)	19.37(0.13)	19.68(0.13)	20.03(0.20)	2013 1129	FLAMINGOS-2	K11
WD 0806−66B ^{b,c}	Y1	> 23.5	> 23.9	2013 1217,1218; 2014 0115,0116,0119	GSAOI	L11
WISE J081117.81−805141.3	T9.5	20.17(0.07)	19.65(0.07)	19.99(0.14)	20.49(0.20)	2013 1126,1129,1206	FLAMINGOS-2	K12
WISEPC J140518.40+553421.5	Y0	21.61(0.12)	2013 0421	NIRI	C11
WISEP J154151.65−225025.2	Y0.5	21.07(0.07)	21.7(0.2)	2013 0508,0511,0805	NIRI	C11
WISEPA J161441.45+173936.7	T9	19.58(0.04)	18.90(0.02)	19.31(0.04)	19.74(0.07)	2013 0404	NIRI	K11
WISE J222055.31−362817.4	Y0	20.91(0.09)	20.64(0.05)	20.96(0.08)	21.33(0.15)	2014 0716	NIRI	K12

^aThe NIRI *Y* magnitudes and FLAMINGOS-2 *K*s have been put on the MKO *Y* and *K* system as described in the text.

^bWhere given, lower limit magnitudes correspond to the limit for a 3σ detection.

^cFor WD 0806−66B a limit of $z_{AB} > 26.2$ was obtained using GMOS-South on 2011 1205, 1230, 1231 and 2012 0119, 0120 and 0121.

Note. — Discovery references are: Cushing et al. 2011; Kirkpatrick et al. 2011, 2012 and 2013; Luhman et al 2011; Mace et al. 2013; Pinfield et al. 2014a.

Table 2. MKO Photometry of WISE Y Dwarfs

Name	Spectral Type	$M - m$ (err) magnitude	Y (err)	J (err)	H (err)	K (err)	Parallax Reference	Photometry Reference	Discovery Reference
WISE J030449.03–270508.3	Y0	20.79(0.09)	21.02(0.16)	P14b	P14b
WISE J035000.32–565830.2	Y1	2.32(0.37)	21.62(0.12)	22.09(0.12)	22.51(0.20)	...	M13	this work	K12
WISE J035934.06–540154.6	Y0	–1.00(0.20)	21.84(0.11)	21.53(0.11)	21.72(0.17)	22.8(0.3)	T14	this work	K12
WISEP J041022.71+150248.5	Y0	1.02(0.12)	19.61(0.04)	19.44(0.03)	20.02(0.05)	19.91(0.07)	B14	Leg13	C11
WISE J053516.80–750024.9	Y1	–0.65(0.41)	22.73(0.30)	22.50(0.20)	23.34(0.34)	T14	M13	this work	K12
WISE J064723.23–623235.5	Y1	0.09(0.18)	23.13(0.09)	22.94(0.10)	> 23.5	> 24	K13,T14	this work	K13
WISE J071322.55–291751.9	Y0	0.18(0.08)	20.34(0.08)	19.98(0.05)	20.19(0.08)	21.30(0.31)	T14	this work	K12
WISE J073444.02–715744.0	Y0	–0.66(0.19)	21.02(0.05)	20.05(0.05)	20.92(0.12)	20.96(0.15)	T14	this work	K12
WD 0806–66B	Y1 ^a	–1.41(0.07)	> 23.5	25.0(0.10) ^b	S09	Luh14b	Luh11
WISE J085510.83–071442.5	Y2 ^a	3.29(0.15)	...	25.0(^{+0.53} _{–0.35}) ^b	L&E	F14	Luh14a
WISEPC J121756.91+162640.2B	Y0	–0.02(0.35)	20.26(0.03)	20.08(0.03)	20.51(0.06)	21.10(0.12)	D13	Liu12	Liu12
WISEPC J140518.40+553421.5	Y0	0.55(0.50)	21.24(0.10)	21.06(0.06)	21.41(0.08)	21.61(0.12)	D13	Leg13, this work	C11
WISEP J154151.65–225025.2	Y0.5	1.22(0.06)	21.46(0.13)	21.12(0.06)	21.07(0.07)	21.7(0.2)	T14	Leg13, this work	C11
WISEP J173835.52+273258.9	Y0	0.54(0.17)	19.86(0.07)	20.05(0.09)	20.45(0.09)	20.58(0.10)	B14	Leg13	C11
WISEP J182831.08+265037.8	Y1.5 ^a	0.13(0.14)	23.03(0.17)	23.48(0.23)	22.73(0.13)	23.48(0.36)	B14	Leg13, this work	C11
WISEPC J205628.90+145953.3	Y0	0.73(0.13)	19.77(0.05)	19.43(0.04)	19.96(0.04)	20.01(0.06)	B14	Leg13	C11
WISE J222055.31–362817.4	Y0	–0.30(0.09)	20.91(0.09)	20.64(0.05)	20.96(0.08)	21.33(0.15)	T14	Leg13	K12

^aSpectral sub-type is uncertain for WD 0806–66B, WISE J085510.83–071442.5 and WISEP J182831.08+265037.8, which have very noisy or no near-infrared spectra.

^bThe J magnitude for WD 0806–66B has been derived from the F110W detection by Luhman et al. (2014b) as described in §2.1. The J magnitude for WISE J085510.83–071442.5 is the FourStar measurement published by Faherty et al. (2014).

Note. — References are: Beichman et al. 2014; Cushing et al. 2011; Dupuy & Kraus 2013; Faherty et al. 2014; Kirkpatrick et al. 2011, 2012 and 2013; Leggett et al. 2013; Liu et al. 2012; Luhman et al 2011; Luhman 2014a; Luhman & Esplin 2014, Luhman et al. 2014b; Marsh et al. 2013; Pinfield et al. 2014b; Subasavage et al. 2009; Tinney et al. 2014; Wright et al. 2014.